A fundamental investigation into the role of beam focal point, and beam divergence, on thermo-capillary stability and evolution in electron beam welding applications

T.F. Flint [a,*], T. Dutilleul [b], W. Kyffin [b]

[a] *The Department of Materials, The University of Manchester, Manchester, UK*
[b] *Nuclear Advanced Manufacturing Research Centre, The University of Sheffield, Rotherham, UK*

ABSTRACT

In this work a novel mathematical framework, that fully describes fusion and vapourisation state transitions in multi-component substrates, has been applied to assist in understanding the fundamental mechanisms of thermo-capillary (keyhole) formation and stability during the electron beam welding process. Specifically the role of electron beam divergence, and the location of the beam focal-point within the substrate, is numerically investigated. It is shown that the location of the beam focal point directly influences the keyhole formation dynamics and leads to drastically different keyhole structures. It is further shown that a less divergent electron beam has a greater penetration rate and produces a more stable thermo-capillary. Finally the chemical heterogeneity induced due to preferential element evaporation during the process is explored and significant Manganese loss is predicted from the simulated SA508 steel substrate.

1. Introduction

Fabricating metallic joints through electron Beam (EB) welding, or other higher energy density processes such as laser or plasma arc welding, presents an exciting opportunity to reduce fabrication costs when compared with traditional arc joining technologies [1,2]. The cost reductions offered by EB welding are particularly attractive during the fabrication of safety-critical, primary-circuit, components for nuclear power generation; where the adoption of higher energy density fabrication technologies offers a step change in the plant construction economics [3,4]. During EB welding, a focused beam of electrons is directed at the towards the surface of a metallic substrate, in a vacuum. The electrons in the beam transfer their kinetic energy to thermal energy upon interacting with the substrate. With sufficient power density, a thermo-capillary, or 'keyhole' is generated through the substrate as the material is vaporised; allowing the beam of electrons to penetrate further into the substrate [5]. This thermo-capillary generation is the mechanism by which this process has such high productivity, as very thick sections may be joined in a single application of the beam. However, the high velocity nature of the fluid and vapour flow within the thermo-capillary means that this structure can be a

source of significant porosity in the finished joint, as vapour bubbles can be entrained within the solidifying material [6–8].

Mathematical modelling of EB welding presents a unique opportunity to understand the fundamental physics responsible for the compositional, topological, microstructural, and thermo-mechanical changes that occur during the process [3,4,9–12]. In fact, the highly transient nature of the flows in EB welding, and materials joined, mean that it is often impossible to accurately observe the flow phenomena experimentally [1]. Mathematical models are also useful in obtaining accurate descriptions of the fabricated joints as the components enter into service; permitting the faithful prediction of safe operating limits, and lifetime evolution of the joint region [4,13]. These mathematical descriptions of the joining process also offer the opportunity to optimise the processes through simulation at a fraction of the cost of an experimental campaign, or to at least narrow the range of parameters investigated experimentally.

Traditional weld modelling approaches neglect the fluid dynamics of the molten and vaporised regions entirely, instead using phenomenological heat source descriptions to represent the complex physics involved in the fluid region and obtain thermal predictions by solving a simple heat conduction problem either numerically or analytically [9,14,15]. These thermal fields are then typically used as the input for a residual stress computation [16,17]. For predictions of the microstructural evolution, phase-field frame-

* Corresponding author.
  E-mail address: Thomas.Flint@manchester.ac.uk (T.F. Flint).

works are preferred for their ability to incorporate a variety of inter-facial physics and bulk kinetics to predict the resultant poly-crystalline structure [11,18–22]. For predictions of the topological evolution, including the fluid flow and macro-scale solidification behaviour, thermal-fluid dynamics frameworks are used that describe the momentum, mass and energy conservation within the domain [3,10,23–26]. Recently this thermal-fluid dynamics approach has been extended to multi-component substrates with an explicit treatment of the vapourisation state transition per chemical species [12,27]; permitting high fidelity simulation of the fusion and vapourisation state transitions in alloys, without the need to fit phenomenological recoil functions, as is done elsewhere [10,28,29]. In this work we will use this recently developed high fidelity, multi-component, framework [27] to numerically investigate the effect of electron beam divergence, and focal position, on the evolution and stability of thermo-capillaries formed during electron beam welding of 5mm thick SA508 ferritic steel substrates. In addition to relating the keyhole formation dynamics to the electron beam characteristics, in terms of beam divergence and focal plane location; the high fidelity numerical framework permits predictions of preferential element evaporation form the substrate during these processes. It will be shown that the framework predicts significant losses of the lighter alloying element components in the substrate, namely Mn and Cr, while the heavier elements with greater vapourisation temperatures are not as significantly perturbed.

2. Method

To mathematically describe the multi-component system, experiencing fusion and vapourisation state transitions, a framework of partial differential equations is used to describe the conservation of momentum, the conservation of energy and the conservation of mass. A description of the framework used in this work can be found elsewhere [12,27]. In this work the description of the heat source has been extended to account for the diverging and oscillating nature of electron beams. The highlights of the mathematical framework will now be briefly presented as well as the description of the spatially varying Gaussian heat flux. The momentum conservation equation is given by:

$$\frac{\partial(\rho \boldsymbol{U})}{\partial t} + \nabla \cdot (\rho \boldsymbol{U} \otimes \boldsymbol{U}) = -\nabla P + \nabla \cdot \boldsymbol{\tau} + \boldsymbol{F_s} + \boldsymbol{F_g} + \boldsymbol{S_m} \qquad (1)$$

where ρ, $\boldsymbol{U}$ and P are the mixture mass density, velocity and pressure respectively. The stress tensor, $\boldsymbol{\tau}$, is given by:

$$\boldsymbol{\tau} = \mu \left[\nabla \boldsymbol{U} + (\nabla \boldsymbol{U})^T \right] - \frac{2}{3} \mu (\nabla \cdot \boldsymbol{U}) \boldsymbol{I}. \qquad (2)$$

Here μ is the mixture-averaged kinematic viscosity. In this work the density changes of the constituent components through vapourisation and condensation is explicitly captured in a mass conservative manner. However, it is assumed that the liquid and vapour states, the density of the components is constant; this choice is made as the density change in the liquid and vapour states is small when compared to the many orders of magnitude change in density that occurs through the vapourisation transition. The source terms $\boldsymbol{F_g}$ and $\boldsymbol{S_m}$ in the momentum conservation equation describe the buoyancy forces and loss of momentum due to solidification of the substrate material within the flow respectively. $\boldsymbol{S_m}$ effectively dampens the momentum to zero in any computational cells where the temperature falls below the mixture averaged liquidus temperature, T_L. ϵ_1 is the volume fraction of components in the fluid (liquid or vapour) states. The surface tension force contributions are found by considering the interactions of all species locally present and their respective, pair-wise, surface ten-

sion coefficients, σ_{kl}:

$$\boldsymbol{F_s} = -\sum_{k=0}^{N} \sum_{l \neq k}^{N} \left[\sigma_{kl} \nabla \cdot \left(\frac{\boldsymbol{\psi}}{|\boldsymbol{\psi}|} \right) \left(\frac{\boldsymbol{\psi}}{|\boldsymbol{\psi}|} \right) + \frac{d\sigma_{kl}}{dT} \left(\nabla T - \frac{\boldsymbol{\psi}}{|\boldsymbol{\psi}|} \left(\frac{\boldsymbol{\psi}}{|\boldsymbol{\psi}|} \cdot \nabla T \right) \right) \right] |\boldsymbol{\psi}| \qquad (3)$$

where $\boldsymbol{\psi} = \alpha_l \nabla \alpha_k - \alpha_k \nabla \alpha_l$, with $\sum_{k=0}^{N} \alpha_k = 1$. The energy conservation in the system is describes through the following transport equation:

$$\frac{\partial(\rho c_p T)}{\partial t} + \nabla \cdot (\boldsymbol{U} c_p \rho T) - \nabla \cdot (k \nabla T) = q$$
$$+ \boldsymbol{\tau} : \nabla \boldsymbol{U} - L_f \left[\frac{\partial(\rho \epsilon_1)}{\partial t} - \nabla \cdot (\boldsymbol{U} \epsilon_1 \rho) \right] - L_v \dot{m}_T \qquad (4)$$

where c_p, T, and k are the mixture heat capacity, temperature, thermal conductivity respectively. L_f and L_v are the latent heats of fusion and vapourisation for the mixture. q is the heat input source representing the electron-beam. In this work a spatially oscillating surface Gaussian distribution is used with the following mathematical description:

$$q = \frac{2.0Q}{\omega^2 \pi} e^{-2 \left(\left(\frac{x - bg}{\omega} \right)^2 + \left(\frac{z - (vt) - lg}{\omega} \right)^2 \right)} \qquad (5)$$

where ω is the distance away from the beam centre, such that the intensity falls to $1/e^2$ of the peak intensity. The beam radius, ω, is also a function of distance along the beam axis [30]. The heat source distribution as a function of depth has the following mathematical form:

$$\omega = \omega_0 \sqrt{1 + \left(\frac{y - \left(y_{focal} - \left(R_y \left(t - t_{shift} \right) \right) \right)}{y_R} \right)^2} \qquad (6)$$

In Eq. 6, y_R is the Rayleigh length and effectively describes the divergence of the beam; as the value of y_R is decreased the profile of the beam becomes more hour-glass in nature. The beam power, Q, and focal point, y_{focal}, are also functions of time. After a time, t_{shift}, the beam power decreases linearly at a rate R_Q, and the focal position traverses in the y-axis at a velocity R_y.

$$Q = max \left(Q_0 - \left(R_Q \left(t - t_{shift} \right) \right), 0 \right) \qquad (7)$$

This behaviour is included in the heat source description to enable the modelling of the power-down process of the electron beam, where the power is decreased and this causes the focal position of the beam to move in tandem. The numerical implementation of this heat source can be seen programatically elsewhere [10].

The mixture averaged properties of the flow are found by a weight fraction sum over the component properties as: $X = \sum_k \alpha_k X_k$ where X is the mixture averaged property to be found, X_k is the phase property of component k, and α_k is the volume fraction of component k, defined as the ratio of the volume of component k in a given cell to the total volume of all components in the cell; $\alpha_k = V_k / \sum_j V_j$. For the thermal conductivity and specific heat, this is further expanded to include the different property values in the solid and liquid state: $X = \sum_k (1 - \epsilon_1) \alpha_k X_{k,s} + \epsilon_1 \alpha_k X_{k,l}$. The final set of equations for the multi-component system are the species fraction transport equations:

$$\frac{\partial(\rho_k \alpha_k)}{\partial t} + \nabla \cdot (\rho_k \boldsymbol{U} \alpha_k) = \nabla \cdot \left(\epsilon_1 \rho D_k \nabla \left(\frac{\rho_k \alpha_k}{\rho} \right) \right) + \dot{m}_k. \qquad (8)$$

In this work, the chemical species present in the domain are decomposed further into condensed and vapourised states. This permits the vapourisation state transition to be properly captured for the multi-component substrate, in a mass conservative manner. $\dot{m}_k$ is then the production rate (positive and negative) of the

k^{th} component in the system. For any given condensed phase, $\dot{m}_k$ is a source term for condensation processes, and a sink term for evaporation processes. In this work we use a simple description of $\dot{m}_k$ given by $r_{vap}\alpha_{liquid}\rho\left(T - T_{vap}\right)/T_{vap}$ for vaporisation and $r_{cond}\alpha_{vapour}\rho\left(T_{vap} - T\right)/T_{vap}$ for condensation. In this work we neglect the pressure dependence on the vapourisation temperature, and assume the vapourisation temperature for each component is constant, although different between the chemical components. Note that diffusion is only considered to occur in the liquid and vapour state. The effective diffusion coefficient D_k of the mixture is found from a weighted summation over the binary diffusion pairs, using a generalised Fickian model. It is assumed that the diffusion coefficients between condensed and vapourised phases is zero, and that the diffusion in the solid state is negligible in relation to diffusion in the fluid. In this manner, by neglecting diffusion between phases with radically different densities, it is reasonable to neglect the higher order diffusion terms from the $\nabla \cdot \left(\rho D_k \nabla\left(\frac{\rho_k \alpha_k}{\rho}\right)\right)$ expression in Eq. 8. The time-scales involved in the processes of interest make these higher order terms negligible. Furthermore, these higher order terms are only relevant when considering diffusion between phases with large density contrast [31]. For the set of multi-component transport equations to be mass conserving, the sum over all phases should reproduce the continuity equation:

$$\underbrace{\sum_k \frac{\partial(\rho_k \alpha_k)}{\partial t}}_{\frac{\partial \rho}{\partial t}} + \underbrace{\sum_k \nabla \cdot (\rho_k \boldsymbol{U} \alpha_k)}_{\nabla \cdot (\rho \boldsymbol{U})} = \underbrace{\sum_k \nabla \cdot \left(\epsilon_1 \rho D_k \nabla\left(\frac{\rho_k \alpha_k}{\rho}\right)\right)}_{=0} + \underbrace{\sum_k \dot{m}_k}_{=0}$$

(9)

It has been shown that this framework is mass conservative through vapourisation and condensation state transitions elsewhere [27].

The governing equations are discretized using the OpenFOAM® library using the cell-centered finite volume approach. The equations are evaluated in an iterative manner, correcting the velocity and pressure fields until convergence is reached, using a PISO (pressure implicit with splitting of operators) approach for multiple iterations at each time step. During the formation of the pressure-Poisson equation, the volumetric dilation due to vapourisation state transitions, $\dot{v}$, are further accounted for. The volume dilation term, and multi-component transport are handled explicitly; requiring extremely small Courant numbers. The multidimensional limiter for explicit solution (MULES) approach is utilised for the solution of the multi-component transport equation. The overall solution procedure used is shown in Algorithm 1.

Validation

Validation of the mathematical framework, and numerical implementation was performed using the common Stefan problem in 1D for a single component pair (liquid and vapour) [32]. The Stefan problem is often chosen as a benchmark problem for assessing the reliability of different liquid-vapour phase change models. The Stefan problem consists of a fluid held at it's particular vapourisation temperature; one side of the domain is then set to a super-heated temperature whilst the other boundary set to the vapourisation temperature. Further details are available elsewhere [32]. In the present case Iso-butane was selected as the working fluid with liquid and vapour density of $\rho_l = 550.6\ kg\,m^{-3}$ and $\rho_v = 9.12\ kg\,m^{-3}$ respectively. The thermal conductivity's and specific heats are $k_v = 1.69 \times 10^{-2}\ kg\,m\,s^{-3}\,K^{-1}$, $k_l = 8.92 \times 10^{-2}\ kg\,m\,s^{-3}\,K^{-1}$, $c_{pv} = 1.816 \times 10^3\ m^2\,s^{-2}\,K^{-1}$, $c_{pl} = 2.446 \times 10^3\ m^2\,s^{-2}\,K^{-1}$ respectively and the latent heat of vapourisation is $L_vap = 3.294 \times 10^5\ m^2\,s^{-2}$. The wall super-heating was $10\ K$, As shown in Fig. 1 the simula-

---

Algorithm 1: Algorithm for the solution of the coupled transport equations in $[t_{n-1}, t_n]$.

Data: $[\boldsymbol{U}]_{t_{n-1}}$, $[P]_{t_{n-1}}$, $[T]_{t_{n-1}}$, $[\boldsymbol{\alpha}]_{t_{n-1}}$
Result: $[\boldsymbol{U}]_{t_n}$, $[P]_{t_n}$, $[T]_{t_n}$, $[\boldsymbol{\alpha}]_{t_n}$
Initialise thermal-fluid dynamics solution: $[\boldsymbol{U}]_{t_n}^0 = [\boldsymbol{U}]_{t_{n-1}}$, $[P]_{t_n}^0 = [P]_{t_{n-1}}$, $[T]_{t_n}^0 = [T]_{t_{n-1}}$ and $[\boldsymbol{\alpha}]_{t_n}^0 = [\boldsymbol{\alpha}]_{t_{n-1}}$;
while $j < N_{PISO}$ **do**
> Using $[\boldsymbol{U}]_{t_n}^j$, solve mixture transport equations (Equation 8) for volume fractions, $[\boldsymbol{\alpha}]_{t_n}^{j+1}$, Return volumetric dilation rate and total latent heat of vapourisation for momentum and energy transport equations;
> Update mixture properties ρ, μ, c_p, k as mass averaged sums using $[\boldsymbol{\alpha}]_{t_n}^{j+1}$;
> Apply first-order domain trace to identify cells to deposit EB energy source;
> Pre-calculate momentum and thermal source terms using $[\boldsymbol{\alpha}]_{t_n}^{j+1}$, $[T]_{t_n}^j$ and $[\boldsymbol{U}]_{t_n}^j$;
> Using $[P]_{t_n}^j$ and pre-calculated source terms, solve Momentum Equation (Equation 1) for the trial velocity field, $[\boldsymbol{U}]_{t_n}^*$;
> Pre-calculate latent heat, using $[T]_{t_n}^j$ and $[\boldsymbol{U}]_{t_n}^j$;
> Solve energy transport equation (Equation 4) for temperature field, $[T]_{t_n}^{j+1}$;
> Using $[\boldsymbol{U}]_{t_n}^*$, solve pressure poisson equation for $[P]_{t_n}^{j+1}$;
> Update the velocity field, $[\boldsymbol{U}]_{t_n}^{j+1}$, by using $[P]_{t_n}^{j+1}$ to project $[\boldsymbol{U}]_{t_n}^*$ onto divergence free space;
> $j = j+1$

end
Update thermal-fluid dynamics solution: $[\boldsymbol{U}]_{t_n} = [\boldsymbol{U}]_{t_n}^j$, $[P]_{t_n} = [P]_{t_n}^j$, $[T]_{t_n} = [T]_{t_n}^j$ and $[\boldsymbol{\alpha}]_{t_n} = [\boldsymbol{\alpha}]_{t_n}^j$;

---

tion results agree very well with the exact analytical solution for the interface location as a function of time.

3. Results

The previously described mathematical framework was utilised to investigate the effect of beam focal point, and beam divergence, on the evolution of the thermo-capillary during electron beam welding of a 5mm thick steel substrate. In all the presented examples material properties were chosen to be representative of SA508 ferritic steel. The material properties used in the simulations are shown in Tables 1 and 2.

In all simulations the beam power has a constant value of $4800\ W$ until the beam is abruptly extinguished at $t = 0.17\ s$. No oscillatory behaviour is included in the results presented in this work. The beam minimum radius has a value of, $\omega_0 = 5 \times 10^{-4}\ m$. In all simulations the beam starting position in the z-direction, and the beam travel velocity are $v = 1.667 \times 10^{-2}\ m\,s^{-1}$ and $l_g = 2 \times 10^{-3}\ m$ respectively. In all presented cases a computational domain of $4 \times 10^{-3}\ m$ in the x-direction by $8 \times 10^{-3}\ m$ in the y-direction by $8 \times 10^{-3}\ m$ in the z-direction was used; with the metallic substrate present between the planes of $y = 1.5 \times 10^{-3}\ m$ and $y = 6.5 \times 10^{-3}\ m$ as can be seen in Fig. 2. The computational domain was regularly discretised into 864,000 cells.

In the first instance, the effect of focal point on keyhole formation dynamics is investigated numerically; key phenomena governing formation and collapse of the thermocapillary are elucidated using the high fidelity numerical framework. Predictions of preferential element loss during the vapourisation state transitions are also presented for one of the scenarios, again, with thorough ex-
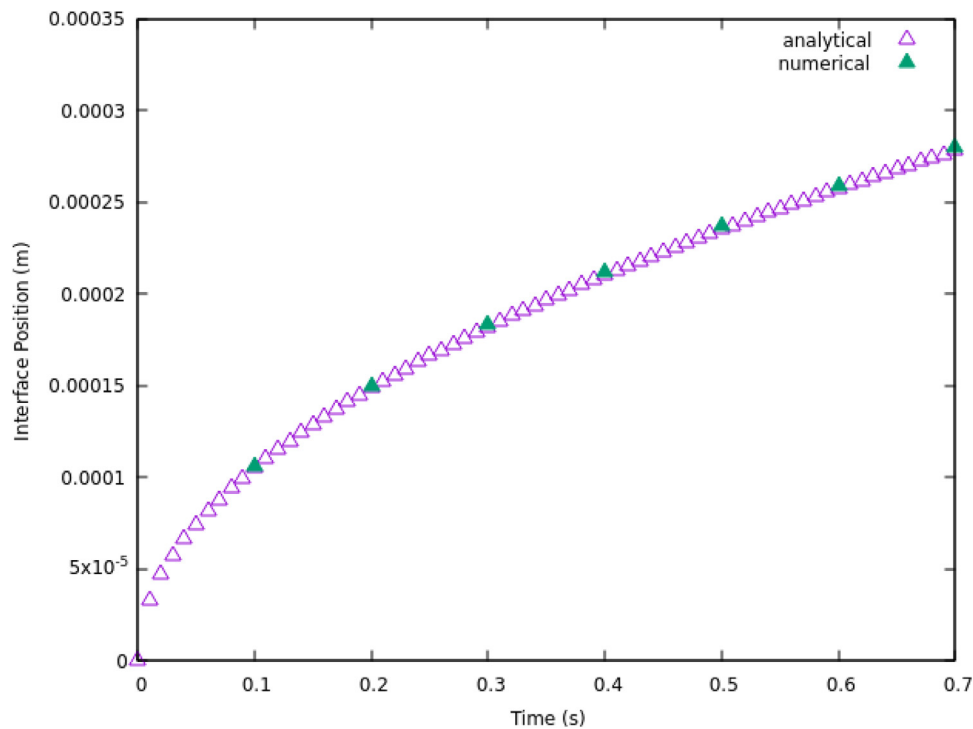
Fig. 1. Comparison of simulation results using the above framework, for a liquid-vapour pair, vs the analytical solution for the Stefan problem.

planation in relation to the governing physics and presented numerical implementation thereof. Finally the role of beam divergence is investigated. It will be shown that the position of the focal point plays a key role in enabling the formation of a thermo-capillary during the process. It will also be shown that lower-divergence beams lead to more stable thermo-capillaries.

3.1. Effect of focal point on thermo-capillary formation during electron beam welding

In this section three scenarios were considered. In each scenario a beam with divergence characterised by a Rayleigh length of $y_R = 2 \times 10^{-3}$ m was directed at the substrate. For each scenario the focal position of the beam was either be in the middle of the 5mm thick substrate, or focused on the top or bottom surfaces of the plate. Fig. 3 shows the evolution of the thermo-capillary for each of these scenarios, with the hour-glass envelope of the beam shown for clarity.

As can be seen from Fig. 2, the position of the beam focal-point has a dramatic effect on the formation and evolution of the

thermo-capillary in the substrate. When the focal point is located at the top surface of the plate, as shown in Fig. 2(a-c), the high power density initially causes rapid formation of a keyhole with a large penetration rate. In this scenario the power density decreases as the beam penetrates through the substrate from the top surface. At 2.3×10^{-3} m the power density is no longer sufficient to generate sufficient vapourisation to form the keyhole any deeper. The result of this is that in this, top-plane focal point, scenario only a partial-penetration thermo-capillary is formed and traverses along the domain as the beam traverses up to a maximum penetration depth of 2.5×10^{-3} m.

When the beam is focused inside the material, as shown in Fig. 2(d-f) the penetration rate is initially lower than the top-plane focal point scenario. However, as the power density is increasing with depth (until the electron beam reaches the mid-plane and then the power density decreases again with depth) in this scenario the rate of keyhole penetration rapidly out-paces this earlier scenario and at 1×10^{-2} : s the thermo-capillary in the middle plane focal point scenario is already at a greater penetration than that of the top-plane focal point scenario. This shows that a

Table 1

Thermo-Physical Properties used in the simulations. The thermal conductivity's for the molten state, k_{liquid}, of *Ni, Mo* and *Cr* are estimated, as little data for these values is present in the literature [33–36].

	Fe	Fe_{vap}	Ni	Ni_{vap}	Cr	Cr_{vap}	Mo	Mo_{vap}	Mn	Mn_{vap}	C	C_{vap}	Ar
$\rho\ [kg\,m^{-3}]$	7874	7.874	8908	8.908	7190	7.19	10,280	10.28	7210	7.210	2000	2.0	1.4
$\nu = \frac{\mu}{\rho}\ [m^2\,s^{-1}]$	$1{\times}10^{-6}$	$5{\times}10^{-6}$	$1{\times}10^{-6}$	$5{\times}10^{-6}$	$1{\times}10^{-6}$	$5{\times}10^{-6}$	$1{\times}10^{-6}$	$5{\times}10^{-6}$	$1{\times}10^{-6}$	$5{\times}10^{-6}$	$1{\times}10^{-6}$	$5{\times}10^{-6}$	$1.48{\times}10^{-5}$
$k_{solid}\ [kg\,m^{-3}\,K^{-1}]$	80.4	-	90.9	-	94.0	-	138.0	-	52.0	-	52.0	-	-
$k_{liquid}\ [kg\,m\,s^{-3}\,K^{-1}]$	30.0	10.0	35.0	10.0	35.0	10.0	50.0	10.0	10.0	10.0	20.0	10.0	0.017
$c_{p_{solid}}\ [m^2\,s^{-2}\,K^{-1}]$	456	-	450	-	450	-	250	-	478	-	709	-	-
$c_{p_{liquid}}\ [m^2\,s^{-2}\,K^{-1}]$	820	1000	730	1000	940	1000	370	1000	500	600.0	750	750.0	521
$T_{melt}\ [K]$	1810	-	1728	-	2180	-	2895	-	1510	-	1750	-	83
$T_{vap}\ [K]$	3134	3134	3000	3000	2944	2944	4912	4912	2334	2334	3915	3915	87
$L_{fus}\ [m^2\,s^{-2}]$	$2.7{\times}10^5$	-	$2.97{\times}10^5$	-	$4.04{\times}10^5$	-	$1.44{\times}10^5$	-	$2.34{\times}10^5$	-	$3.0{\times}10^5$	-	-
$L_{vap}\ [m^2\,s^{-2}]$	-	$6.09{\times}10^6$	-	$6.52{\times}10^6$	-	$6.67{\times}10^6$	-	$4.15{\times}10^6$	-	$4.02{\times}10^6$	-	$9.75{\times}10^6$	-
$m\ [kg\,mol^{-1}]$	0.055	0.055	0.058	0.058	0.052	0.052	0.096	0.096	0.055	0.055	0.012	0.012	0.04
$\beta\ [K^{-1}]$	$1{\times}10^{-5}$	$5{\times}10^{-4}$	$1{\times}10^{-5}$	$5{\times}10^{-4}$	$1{\times}10^{-5}$	$5{\times}10^{-4}$	$1{\times}10^{-5}$	$5{\times}10^{-4}$	$1{\times}10^{-5}$	$5{\times}10^{-4}$	$1{\times}10^{-5}$	$5{\times}10^{-4}$	$5{\times}10^{-4}$

Table 2

Pair-wise parameters used in the present simulations. Note that where values were not available in the literature, they were estimated from available values.[33–36].

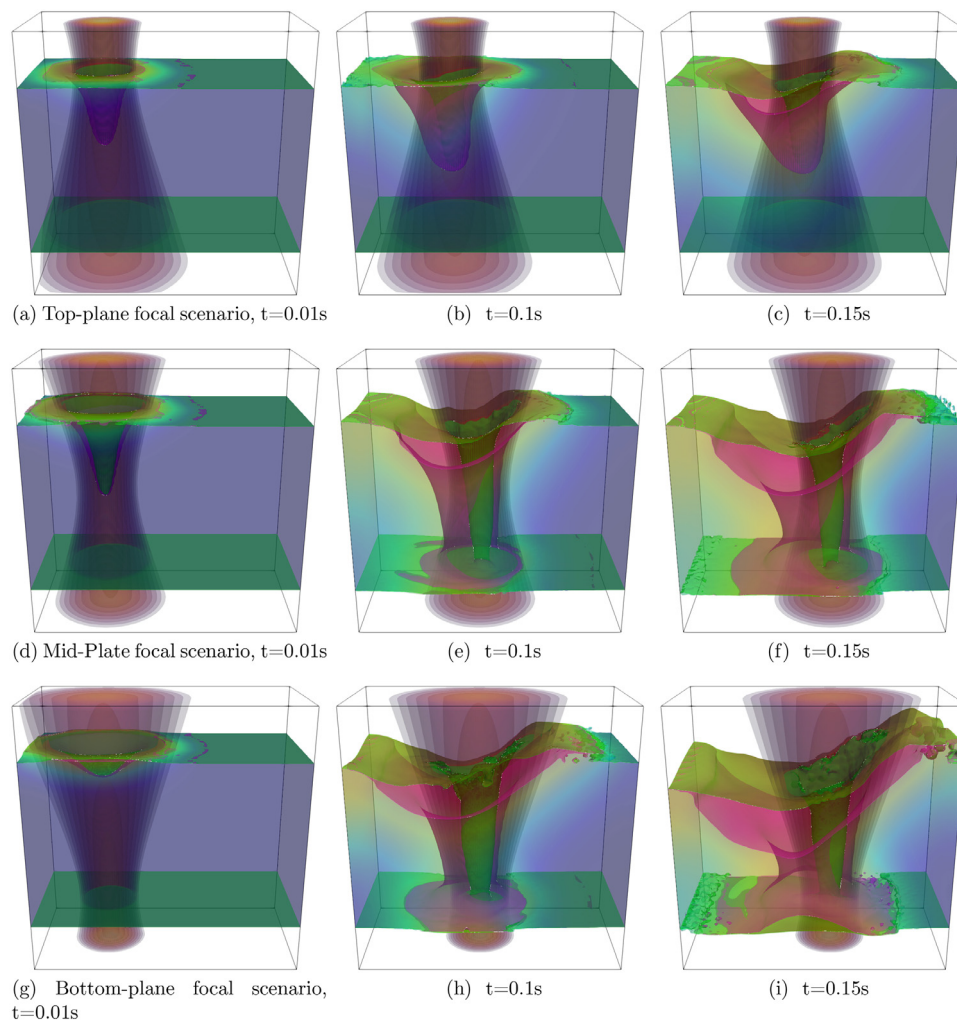| $\begin{pmatrix} \sigma_{ij}\,[N\,m^{-1}] \\ d\sigma_{ij}/dT\,[N\,m^{-1}\,K^{-1}] \\ D_{ij}\,[m^2\,s^{-1}] \end{pmatrix}$	Fe_{vap}	Ni	Ni_{vap}	Cr	Cr_{vap}	Mo	Mo_{vap}	Mn	Mn_{vap}	C	C_{vap}	Ar
Fe	$\begin{pmatrix} 1.8 \\ -1\times10^{-4} \\ 0 \end{pmatrix}$	$\begin{pmatrix} 0 \\ 0 \\ 2\times10^{-9} \end{pmatrix}$	$\begin{pmatrix} 1.8 \\ -1\times10^{-4} \\ 0 \end{pmatrix}$	$\begin{pmatrix} 0 \\ 0 \\ 1\times10^{-9} \end{pmatrix}$	$\begin{pmatrix} 1.8 \\ -1\times10^{-4} \\ 0 \end{pmatrix}$	$\begin{pmatrix} 0 \\ 0 \\ 1\times10^{-9} \end{pmatrix}$	$\begin{pmatrix} 1.8 \\ -1\times10^{-4} \\ 0 \end{pmatrix}$	$\begin{pmatrix} 0 \\ 0 \\ 3\times10^{-9} \end{pmatrix}$	$\begin{pmatrix} 1.8 \\ -1\times10^{-4} \\ 0 \end{pmatrix}$	$\begin{pmatrix} 0 \\ 0 \\ 5\times10^{-10} \end{pmatrix}$	$\begin{pmatrix} 1.8 \\ -1\times10^{-4} \\ 0 \end{pmatrix}$	$\begin{pmatrix} 1.8 \\ -1\times10^{-4} \\ 0 \end{pmatrix}$
Fe_{vap}		$\begin{pmatrix} 1.7 \\ -1\times10^{-5} \\ 0 \end{pmatrix}$	$\begin{pmatrix} 0 \\ 0 \\ 1\times10^{-7} \end{pmatrix}$	$\begin{pmatrix} 1.6 \\ -1\times10^{-5} \\ 0 \end{pmatrix}$	$\begin{pmatrix} 0 \\ 0 \\ 1\times10^{-7} \end{pmatrix}$	$\begin{pmatrix} 2.2 \\ -1\times10^{-5} \\ 0 \end{pmatrix}$	$\begin{pmatrix} 0 \\ 0 \\ 1\times10^{-7} \end{pmatrix}$	$\begin{pmatrix} 2.2 \\ -1\times10^{-5} \\ 0 \end{pmatrix}$	$\begin{pmatrix} 0 \\ 0 \\ 1\times10^{-7} \end{pmatrix}$	$\begin{pmatrix} 2.2 \\ -1\times10^{-5} \\ 0 \end{pmatrix}$	$\begin{pmatrix} 0 \\ 0 \\ 1\times10^{-7} \end{pmatrix}$	$\begin{pmatrix} 0 \\ 0 \\ 1\times10^{-7} \end{pmatrix}$
Ni			$\begin{pmatrix} 1.7 \\ -1\times10^{-5} \\ 0 \end{pmatrix}$	$\begin{pmatrix} 0 \\ 0 \\ 1.5\times10^{-9} \end{pmatrix}$	$\begin{pmatrix} 1.7 \\ -1\times10^{-5} \\ 0 \end{pmatrix}$	$\begin{pmatrix} 0 \\ 0 \\ 1\times10^{-9} \end{pmatrix}$	$\begin{pmatrix} 1.7 \\ -1\times10^{-5} \\ 0 \end{pmatrix}$	$\begin{pmatrix} 0 \\ 0 \\ 8\times10^{-10} \end{pmatrix}$	$\begin{pmatrix} 1.7 \\ -1\times10^{-5} \\ 0 \end{pmatrix}$	$\begin{pmatrix} 0 \\ 0 \\ 5\times10^{-10} \end{pmatrix}$	$\begin{pmatrix} 1.7 \\ -1\times10^{-5} \\ 0 \end{pmatrix}$	$\begin{pmatrix} 1.7 \\ -1\times10^{-4} \\ 0 \end{pmatrix}$
Ni_{vap}				$\begin{pmatrix} 1.6 \\ -1\times10^{-5} \\ 0 \end{pmatrix}$	$\begin{pmatrix} 0 \\ 0 \\ 1\times10^{-7} \end{pmatrix}$	$\begin{pmatrix} 2.2 \\ -1\times10^{-5} \\ 0 \end{pmatrix}$	$\begin{pmatrix} 0 \\ 0 \\ 1\times10^{-7} \end{pmatrix}$	$\begin{pmatrix} 2.2 \\ -1\times10^{-5} \\ 0 \end{pmatrix}$	$\begin{pmatrix} 0 \\ 0 \\ 1\times10^{-7} \end{pmatrix}$	$\begin{pmatrix} 2.2 \\ -1\times10^{-5} \\ 0 \end{pmatrix}$	$\begin{pmatrix} 0 \\ 0 \\ 1\times10^{-7} \end{pmatrix}$	$\begin{pmatrix} 0 \\ 0 \\ 1\times10^{-7} \end{pmatrix}$
Cr					$\begin{pmatrix} 1.6 \\ -1\times10^{-5} \\ 0 \end{pmatrix}$	$\begin{pmatrix} 0 \\ 0 \\ 1\times10^{-9} \end{pmatrix}$	$\begin{pmatrix} 1.6 \\ -1\times10^{-5} \\ 0 \end{pmatrix}$	$\begin{pmatrix} 0 \\ 0 \\ 8\times10^{-10} \end{pmatrix}$	$\begin{pmatrix} 1.6 \\ -1\times10^{-5} \\ 0 \end{pmatrix}$	$\begin{pmatrix} 0 \\ 0 \\ 5\times10^{-10} \end{pmatrix}$	$\begin{pmatrix} 1.6 \\ -1\times10^{-5} \\ 0 \end{pmatrix}$	$\begin{pmatrix} 1.6 \\ -1\times10^{-4} \\ 0 \end{pmatrix}$
Cr_{vap}						$\begin{pmatrix} 2.2 \\ -1\times10^{-5} \\ 0 \end{pmatrix}$	$\begin{pmatrix} 0 \\ 0 \\ 1\times10^{-7} \end{pmatrix}$	$\begin{pmatrix} 2.2 \\ -1\times10^{-5} \\ 0 \end{pmatrix}$	$\begin{pmatrix} 0 \\ 0 \\ 1\times10^{-7} \end{pmatrix}$	$\begin{pmatrix} 2.2 \\ -1\times10^{-5} \\ 0 \end{pmatrix}$	$\begin{pmatrix} 0 \\ 0 \\ 1\times10^{-7} \end{pmatrix}$	$\begin{pmatrix} 0 \\ 0 \\ 1\times10^{-7} \end{pmatrix}$
Mo							$\begin{pmatrix} 2.2 \\ -1\times10^{-5} \\ 0 \end{pmatrix}$	$\begin{pmatrix} 0 \\ 0 \\ 8\times10^{-10} \end{pmatrix}$	$\begin{pmatrix} 2.2 \\ -1\times10^{-5} \\ 0 \end{pmatrix}$	$\begin{pmatrix} 0 \\ 0 \\ 5\times10^{-10} \end{pmatrix}$	$\begin{pmatrix} 1.5 \\ -1\times10^{-5} \\ 0 \end{pmatrix}$	$\begin{pmatrix} 2.0 \\ -1\times10^{-4} \\ 0 \end{pmatrix}$
Mo_{vap}								$\begin{pmatrix} 1.5 \\ -1\times10^{-5} \\ 0 \end{pmatrix}$	$\begin{pmatrix} 0 \\ 0 \\ 1\times10^{-7} \end{pmatrix}$	$\begin{pmatrix} 1.0 \\ -1\times10^{-5} \\ 0 \end{pmatrix}$	$\begin{pmatrix} 0 \\ 0 \\ 1\times10^{-7} \end{pmatrix}$	$\begin{pmatrix} 0 \\ 0 \\ 1\times10^{-7} \end{pmatrix}$
Mn									$\begin{pmatrix} 1.5 \\ -1\times10^{-5} \\ 0 \end{pmatrix}$	$\begin{pmatrix} 0 \\ 0 \\ 5\times10^{-10} \end{pmatrix}$	$\begin{pmatrix} 1.5 \\ -1\times10^{-5} \\ 0 \end{pmatrix}$	$\begin{pmatrix} 1.5 \\ -1\times10^{-4} \\ 0 \end{pmatrix}$
Mn_{vap}										$\begin{pmatrix} 2.0 \\ -1\times10^{-5} \\ 0 \end{pmatrix}$	$\begin{pmatrix} 0 \\ 0 \\ 1\times10^{-7} \end{pmatrix}$	$\begin{pmatrix} 0 \\ 0 \\ 1\times10^{-7} \end{pmatrix}$
C											$\begin{pmatrix} 1.5 \\ -1\times10^{-5} \\ 0 \end{pmatrix}$	$\begin{pmatrix} 1.5 \\ -1\times10^{-4} \\ 0 \end{pmatrix}$
C_{vap}												$\begin{pmatrix} 0 \\ 0 \\ 1\times10^{-7} \end{pmatrix}$

Fig. 2. Time evolution of thermo-capillary structure and substrate penetration as a function of electron beam focal point within the domain for the same beam divergence. The envelope of the electron beam heat source is shown for clarity. The magenta and lime-green isosurfaces delimit the solid-liquid and liquid-vapour states respectively. (For interpretation of the references to colour in this figure legend, the reader is referred to the web version of this article.)

level of under-focusing of the beam is preferable to achieve deeper penetrations.

It can be seen that in the scenario with the focal point located at the bottom plane of the substrate, shown in Fig. 2(g-i), the thermo-capillary is initially slow to form as the power density at the top surface (where the beam first interacts with the substrate) is lowest. In this scenario the power density of the beam increases with depth at all positions through the domain.

Comparing the full penetration scenarios, where the focal point is at the mid-plane and bottom-plane of the substrate - shown in Fig. 2(d-f) and 2(g-i) respectively - it can be seen that there has been more substrate loss in the bottom-plane focal point scenario. This is due to a combination of factors. with the focal point at the bottom plane, the wider beam radius at the top-plane of the substrate means that a larger area of substrate ahead of the beam is pre-heated. This results in a larger radii keyhole in this scenario. The large magnitude velocity fields then carry a greater proportion of the metallic vapour out of the computational domain in this bottom-plane focal point scenario. With the focal point located at the bottom-plane, it can also be seen that there is a greater degree of heterogeneity in the structure of the liquid-vapour interface; the disturbances on this surface are the very structures that will trap vapour bubbles or non-condensing gas bubbles in the process and lead to porosity formation.

As previously described the state transition from the liquid to vapour state, and associated step change in density between these states creates a large volumetric expansion, and associated large magnitude velocity field, that exerts a recoil force on the walls of the keyhole. The recoil effect, along with surface tension, stabilises the thermo-capillary against collapse. Once the heat source is extinguished, the rate at which liquid substrate material is converted into metallic vapour drastically decreases, and eventually becomes zero; as the temperature falls below the vapourisation temperature for all components. Fig. 3 shows how the velocity profile in the thermo-capillary, for the mid-plane focal point scenario, changes once the heat source is extinguished. In this scenario the heat source is extinguished immediately after $t = 0.17$ s.

It can be seen in Fig. 3 that the velocity field drastically changes once the heat source is extinguished. Observing the streamlines at $t = 0.17$ s when the heat source is still active, it can be observed that there are regions where the velocity field is directed away from the liquid/vapour interface into the vapour state; at these locations vapourisation is occurring. The velocity magnitude is much greater whilst the heat source is active. Once the heat source is extinguished, the recoil effect within the keyhole gradually decreases with time as the local temperature field at the liquid/vapour interface decreases below the respective vapourisation temperatures of the components. Additionally, components in their
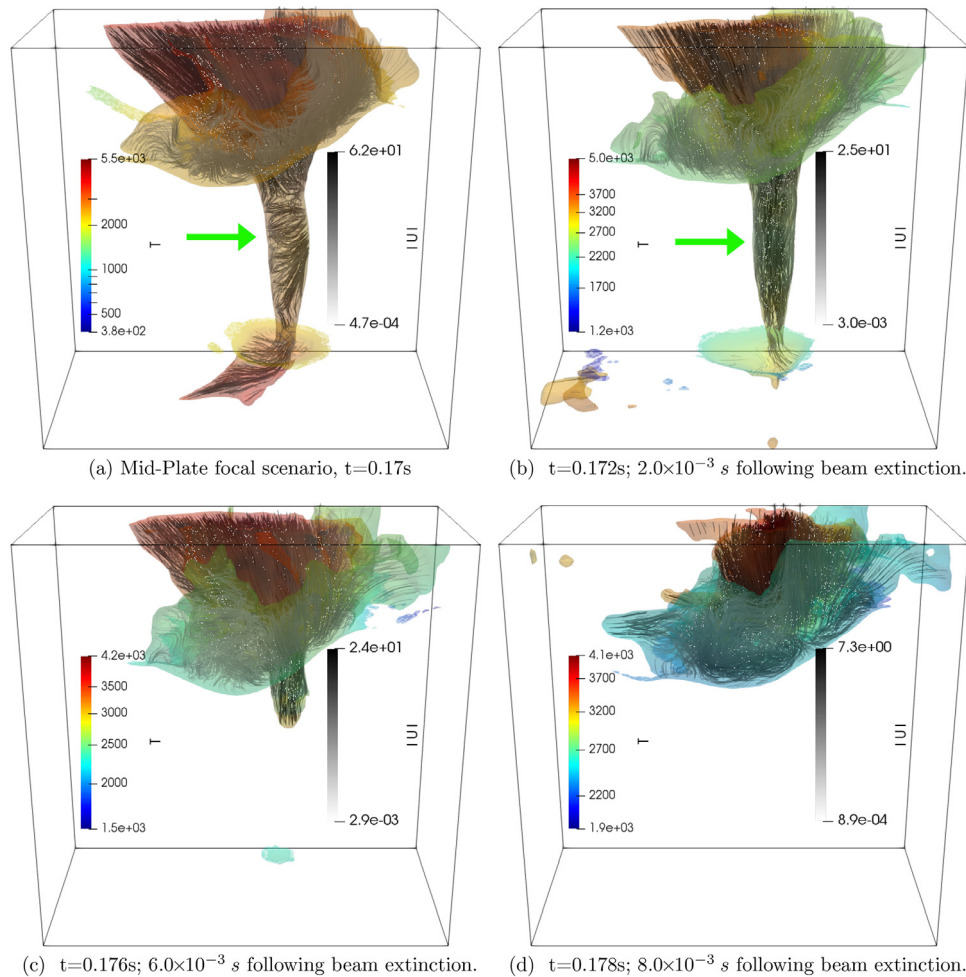
(a) Mid-Plate focal scenario, t=0.17s

(b) t=0.172s; 2.0×10^{-3} s following beam extinction.

(c) t=0.176s; 6.0×10^{-3} s following beam extinction.

(d) t=0.178s; 8.0×10^{-3} s following beam extinction.

Fig. 3. Velocity and temperature field in the thermo-capillary during the keyhole collapse phase of the simulated electron beam welding process. Here the streamlines in the multi-component vapour phases are plotted in grey-scale with a translucent temperature field. The volumetric expansion that occurs as the multi-component metallic substrate goes through the vapourisation state transition induces a large magnitude velocity field in the vapour plume whilst the heat source is active; stabilising the thermo-capillary. After the heat source is extinguished immediately after $t = 0.17$ s the thermo-capillary begins to collapse. Highlighted with the green arrows are the transition areas of interest from a more to less vortical flow field after heat source extinction. (For interpretation of the references to colour in this figure legend, the reader is referred to the web version of this article.)

vapour state will begin to condense into their liquid states as the temperature decreases. Without the effect of vapourisation recoil, the main mechanism by which the thermo-capillary is maintained is no longer present and the keyhole begins to collapse. It can be seen that as the degree of vapourisation decreases, the vorticity (a measure of twist in the velocity field) significantly decreases and the streamlines become more aligned. It can be seen from Fig. 3 that in this scenario the walls of the keyhole make contact at the base of the structure, as liquid metal flows down the side-walls due to gravity, surface tension, and the lack of recoil effects. Once the liquid metal bridges the keyhole at the base of the domain, surface tension effects pull the remainder of the thermo-capillary structure together until the keyhole structure has completely collapsed at approximately $t = 0.178$ s. This demonstrates that the thermo-capillary structure collapses quickly, in 8×10^{-3} s in this mid-plane focal point scenario.

While the main focus of this work is on the formation and stability of the thermo-capillary during the electron beam process; the mathematical framework that is used here - and is required for the proper treatment of these problems - decomposes the substrate into multiple chemical components in the condensed and vapourised states. This allows the mathematical treatment, and prediction, of preferential element evaporation in these processes. It is known experimentally that certain elements

vapourise at lower temperatures and greater rates for a given super-heating above their respective vapourisation temperatures [37]. Fig. 4 shows the path and component fractions of the condensed states corresponding to the later stages of the mid-plane focal point scenario at $t = 0.21$ s.

In Fig. 4 it can be seen that the thermo-capillary induces significant perturbations in the alloying elements. It can be seen that the elements Mn and Cr have experienced preferential loss from the substrate where the keyhole propagated. Note from Table 1 that Mn and Cr have the lowest vapourisation temperatures of the elements included in the substrate. As described previously, the mass transfer rate between the liquid and vapour states for any chemical species is proportional to the super-heating (or super-cooling in the case of condensation). Therefore the elements with a lower vapourisation temperature will have a greater transformation rate ($\dot{m}_k$) when the multi-component substrate is exposed to a high energy density source of heat, such as the electron-beam source, that induces locally high temperatures. This is the mechanism by which elements with lower vapourisation temperatures are predicted to evaporate preferentially in multi-component substrates. Similarly, as the vapour plume exits the keyhole, the components with the greatest vapourisation temperature will tend to condense first onto the keyhole side-walls and be re-absorbed into the liquid. This loss prediction is in agreement with reported behaviour
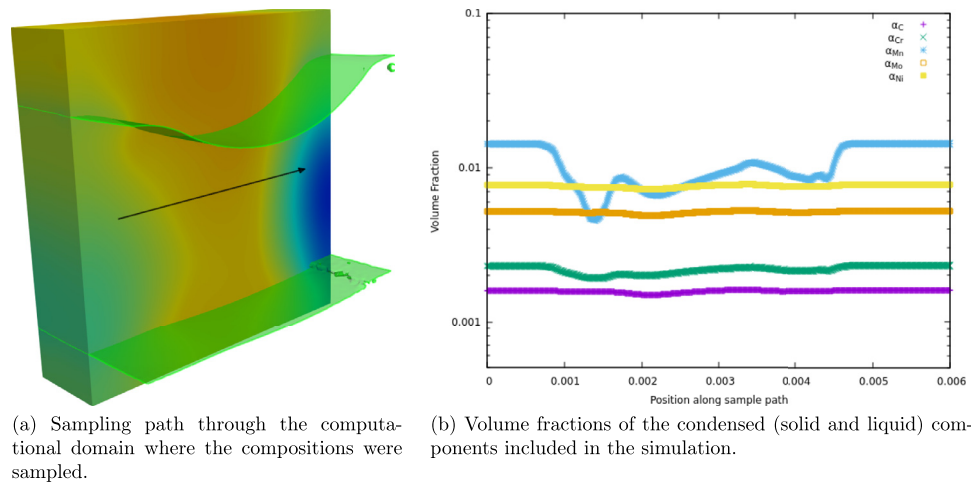
(a) Sampling path through the computational domain where the compositions were sampled.

(b) Volume fractions of the condensed (solid and liquid) components included in the simulation.

Fig. 4. Compositional changes predicted in the substrate at $t = 0.21$ s, following complete collapse of the thermo-capillary due to beam extinction at $t = 0.17$ s. The Mn component is expected to be preferentially lost from the substrate due to a combination of a lower vapourisation temperature and vapourisation rate. The lime-green isosurface delimits the condensed (solid and liquid) from the non-condensed (vapour and gas) phases. (For interpretation of the references to colour in this figure legend, the reader is referred to the web version of this article.)

elsewhere in the literature [37]. An animation of the keyhole formation, progression, and collapse is included with this submission for this case where the beam focal point is placed at the mid-plane of the substrate.

3.2. Effect of beam divergence on thermo-capillary formation and stability

In this section we take the case where the beam was focused on the top surface of the domain (from the previous section) where a full penetration thermo-capillary failed to form, and investigate the effect of reducing the beam divergence on the formation dynamics of the thermo-capillary. Two additional scenarios are considered where the beam divergence parameter, y_R, is set to $y_R = 5 \times 10^{-3}$ m and $y_R = 1 \times 10^{-2}$ m respectively. Fig. 5 shows the time-evolution of the thermo-capillary, and beam envelope, for these scenarios as well as the original $y_R = 2 \times 10^{-3}$ m scenario.

It can be seen in Fig. 5 that as the divergence of the beam is decreased, and the power density becomes more uniform along the beam axis, the thermo-capillary is able to penetrate the entire thickness of the substrate. It is interesting to note that although the beam achieves 'full penetration' in the intermediate divergence scenario with $y_R = 5 \times 10^{-3}$ m the keyhole is unstable and periodically partially collapses and re-forms. Fig. 5c shows the remnants of one of these keyhole collapse events with the beam re-forming the thermo-capillary structure above a vapour bubble that was 'cut-off' during the keyhole collapse. Fig. 5(e-f) shows that with further decrease in the beam divergence the keyhole achieved full penetration and was stable throughout the traverse along the substrate.

4. Discussion

In electron beam welding applications the formation of a stable thermo-capillary is essential to mitigate against porosity generation in the joint region. It is known that the collapsing thermo-capillary, such as occurs at the end of the EB weld as the power is decreased, leads to a higher propensity of porosity formation and inclusion in these regions. Furthermore, the diverging nature of the electron beam, generating a heat source profile with an hour-glass envelope, has a significant effect on the keyhole formation dynamics as the power density can vary significantly along

the beam axis. Understanding the governing mechanisms behind the keyhole formation and collapse requires mathematical frameworks capable of capturing the fundamental physics of the process. The utilisation of a physically robust modelling framework, that fully captures the volumetric dilation during the vapourisation/condensation transitions ($\frac{1}{\rho}\frac{D\rho}{Dt} = \nabla \cdot \boldsymbol{U}$), the diverging nature of the electron beam with depth, and the multi-component nature of the typical alloy substrates used in electron beam welding applications ensures a more complete physical description of such processes are obtained. However, it must be noted that the higher fidelity modelling comes at the cost of significantly greater computational cost when compared with lower fidelity modelling approaches. In this work we do not consider the effects of acceleration voltage and current explicitly, these two effects are simply grouped into the beam power term. However, it is known that the accelerating voltage is closely related to the observed beam divergence, and therefore the Rayleigh length parameter; this coupling warrants further exploration in the future. Furthermore, the linear interpolation approximation of many of the material properties should ideally be linked to thermodynamic databases. This thermodynamic informed material properties approach will be pursued in the future.

In the electron beam welding scenarios presented here, it is shown that the focal position and beam divergence are critical parameters that govern the initiation and maintenance of the keyhole. It is also shown that as the thermo-capillary collapses due to heat source extinction, the velocity field dramatically reduces in magnitude, and becomes significantly less vortical. Furthermore, the presented framework is used to predict preferential element losses from the substrate. It is predicted that Mn and Cr will be lost from the substrate due to their lower vapourisation temperature and higher transition rate.

The ultimate goal of the simulation work presented here is to aid in welding procedure optimisation to mitigate against porosity formation in electron beam welding applications. The stability of the keyhole is not the only consideration for porosity mitigation; All thermo-capillaries must collapse as the power is decreased at the end of joints, and so all thermo-capillaries go through a highly transient closure. In addition to the stability, other considerations must be made. For example, the proportion of liquid metal surrounding the keyhole is thought to play an important role in mitigating against porosity inclusion; a greater proportion of liquid metal on the keyhole sidewalls means that when the
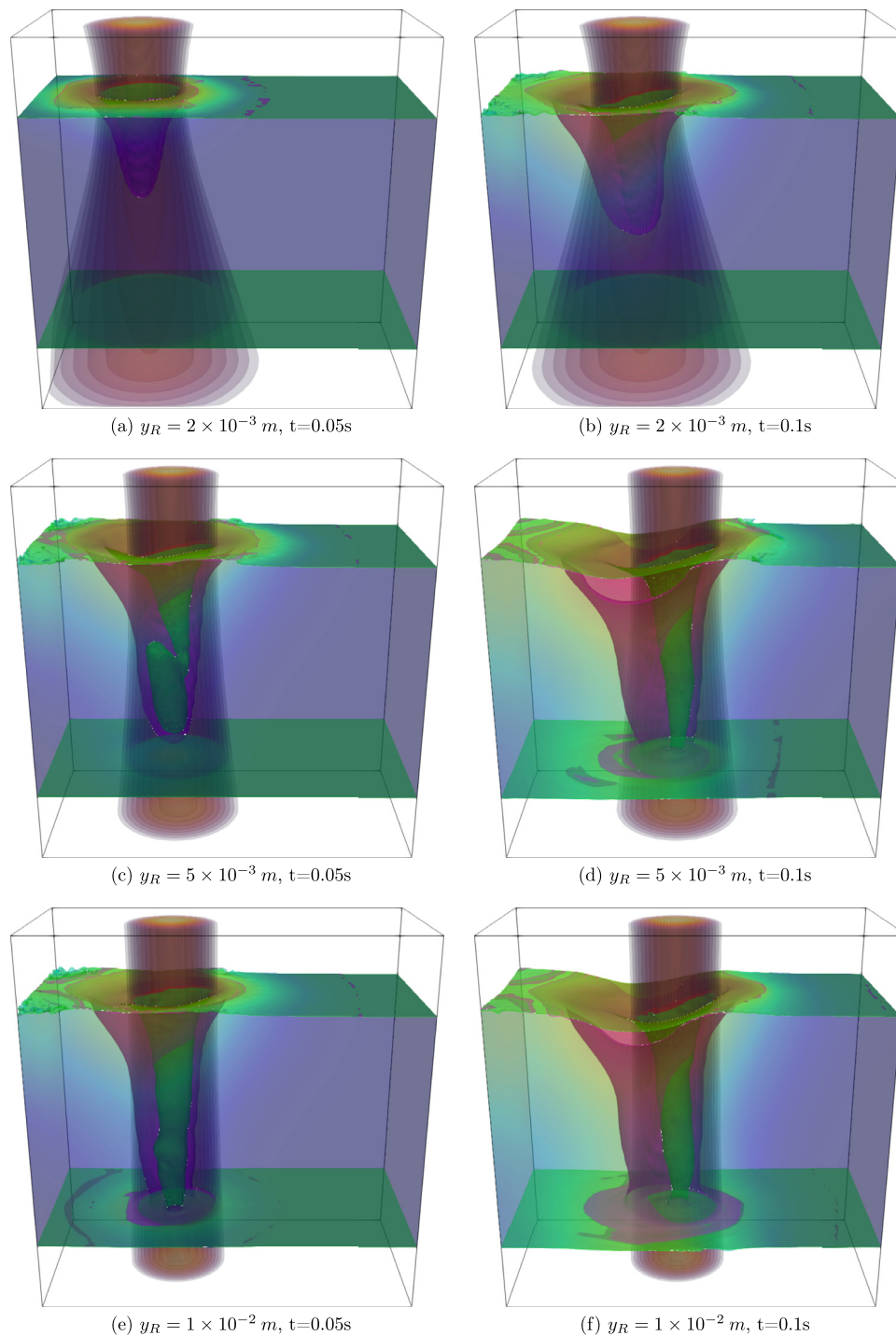
(a) $y_R = 2 \times 10^{-3}\ m$, t=0.05s

(b) $y_R = 2 \times 10^{-3}\ m$, t=0.1s

(c) $y_R = 5 \times 10^{-3}\ m$, t=0.05s

(d) $y_R = 5 \times 10^{-3}\ m$, t=0.1s

(e) $y_R = 1 \times 10^{-2}\ m$, t=0.05s

(f) $y_R = 1 \times 10^{-2}\ m$, t=0.1s

Fig. 5. Time evolution of thermo-capillary formation for three different beam divergence characteristics. A lower beam divergence results in a higher propensity to form a full-penetration keyhole. The magenta and lime-green isosurfaces delimit the solid-liquid and liquid-vapour states respectively. (For interpretation of the references to colour in this figure legend, the reader is referred to the web version of this article.)

thermo-capillary does collapse, there is a greater probability of any entrained porosity bubbles to escape the substrate before being caught by the advancing solidification front. It can be seen in the presented simulations that placing the focal point of the beam further into the substrate produces a keyhole surrounded by a greater volume of liquid metal. More work is required in this area - particularly at greater substrate thicknesses - but it is hypothesised, based on the results of this work, that it is preferable that zipping the thermo-capillary up from the base results in a final joint with minimal porosity inclusion.

5. Conclusions

In this work we show that during the electron beam welding, of a multi-component metallic substrate, the focal point of the beam, and beam divergence govern the formation and stability of thermo-capillaries. It is shown that changing the focal position from being located at the top-surface of the substrate, to being located mid-depth or located at the bottom surface, a full penetration thermo-capillary can be generated, instead of a partial penetration thermo-capillary; demonstrating that under-focusing of the

beam is a crucial component for successful EB welding procedure development. Furthermore, it is shown that decreasing the beam divergence leads to a higher propensity to generate greater penetration keyholes; although during the transition from partial to full-penetration, through decreasing of the divergence, it is shown that some instabilities indeed form at intermediate beam divergences. While the compositional changes in the substrate due to preferential element evaporation during the electron beam welding process are not the primary focus of this work, it is also predicted that in the SA508 substrate considered, we expect to see significant Mn loss; this will be explored further in the future. Specific summarised conclusions to this work are as follows:

1. The location of the beam focal point determines the penetration rate and total penetration for beam power densities that are not sufficient to always fully penetrate the substrate.
2. As the focal point is moved to be at the bottom (far) face of the substrate, larger thermo-capillaries are generated and more material ablation is observed.
3. As the beam divergence is decreased, full penetration keyholes are more likely to form. However, in the transition from partial to full penetration, these keyholes are more likely to be unstable.
4. Significant Mn, and to a lesser extent Cr, evaporation is predicted for the electron beam welding of SA508 ferritic steel.

Declaration of Competing Interest

The Authors declare that there is no competing interest

CRediT authorship contribution statement

T.F. Flint: Conceptualization, Data curation, Formal analysis, Investigation, Methodology, Project administration, Resources, Software, Validation, Visualization, Writing – original draft, Writing – review & editing. **T. Dutilleul:** Conceptualization, Formal analysis, Funding acquisition, Investigation, Supervision. **W. Kyffin:** Funding acquisition, Project administration, Resources, Supervision.

Data availability

The authors declare that the data supporting the findings of this study are available from the corresponding author upon reasonable request.

Acknowledgements

Supplementary material

Supplementary material associated with this article can be found, in the online version, at doi:10.1016/j.ijheatmasstransfer. 2023.124262.

References

[1] L. Aucott, H. Dong, W. Mirihanage, R. Atwood, A. Kidess, S. Gao, S. Wen, J. Marsden, S. Feng, M. Tong, T. Connolley, M. Drakopoulos, C.R. Kleijn, I.M. Richardson, D.J. Browne, R.H. Mathiesen, H.V. Atkinson, Revealing internal flow behaviour in arc welding and additive manufacturing of metals, Nat. Commun. (2018), doi:10.1038/s41467-018-07900-9.

[2] J.A. Francis, H.K.D.H. Bhadeshia, P.J. Withers, Welding residual stresses in ferritic power plant steels, Mater. Sci. Technol. 23 (9) (2007) 1009–1020, doi:10.1179/174328407X213116.

[3] S. Borrmann, C. Kratzsch, L. Halbauer, A. Buchwalder, H. Biermann, I. Saenko, K. Chattopadhyay, R. Schwarze, Electron beam welding of CrMnNi-steels: CFD-modeling with temperature sensitive thermophysical properties, Int. J. Heat. Mass. Transf 139 (2019) 442–455, doi:10.1016/J.IJHEATMASSTRANSFER.2019.04.125.

[4] A.N. Vasileiou, M.C. Smith, J. Balakrishnan, J.A. Francis, C.J. Hamelin, The impact of transformation plasticity on the electron beam welding of thick-section ferritic steel components, Nucl. Eng. Des. (2017), doi:10.1016/j.nucengdes.2017.03.040.

[5] S.F. Su, H.K. Lin, J.C. Huang, N.J. Ho, Electron-beam welding behavior in Mg-Al-based alloys, Metall. Mater. Trans. A 33 (5) (2002) 1461–1473.

[6] H. Zhao, W. Niu, B. Zhang, Y. Lei, M. Kodama, T. Ishide, Modelling of keyhole dynamics and porosity formation considering the adaptive keyhole shape and three-phase coupling during deep-penetration laser welding, J. Phys. D. Appl. Phys. 44 (48) (2011), doi:10.1088/0022-3727/44/48/485302.

[7] N. Seto, S. Katayama, A. Matsunawa, Porosity formation mechanism and suppression procedure in laser welding of aluminum alloy, Yosetsu Gakkai Ronbunshu/Quarterly Journal of the Japan Welding Society (2000), doi:10.2207/qjjws.18.243.

[8] S. Pang, X. Chen, X. Shao, S. Gong, J. Xiao, Dynamics of vapor plume in transient keyhole during laser welding of stainless steel: local evaporation, plume swing and gas entrapment into porosity, Opt. Lasers Eng. (2016), doi:10.1016/j.optlaseng.2016.01.019.

[9] T. Flint, J. Francis, M. Smith, A.N. Vasileiou, Semi-analytical solutions for the transient temperature fields induced by a moving heat source in an orthogonal domain, Int. J. Therm. Sci. 123 (2018) 140–150, doi:10.1016/J.IJTHERMALSCI.2017.09.012.

[10] T.F. Flint, G. Parivendhan, A. Ivankovic, M.C. Smith, P. Cardiff, Beamweldfoam: numerical simulation of high energy density fusion and vapourisation-inducing processes, SoftwareX 18 (2022) 101065, doi:10.1016/j.softx.2022.101065.

[11] T.F. Flint, Y.L. Sun, Q. Xiong, M.C. Smith, J.A. Francis, Phase-Field simulation of grain boundary evolution in microstructures containing second-Phase particles with heterogeneous thermal properties, Sci. Rep. 9 (1) (2019) 18426, doi:10.1038/s41598-019-54883-8.

[12] T. Flint, L. Scotti, H. Basoalto, M. Smith, A thermal fluid dynamics framework applied to multi-component substrates experiencing fusion and vaporisation state transitions, Commun. Phys. 3 (1) (2020), doi:10.1038/s42005-020-00462-7.

[13] M.C. Smith, A. Smith, C. Ohms, R. Wimpory, A review of the NeT TG4 international weld residual stress benchmark, in: ASME 2015 Pressure Vessels and Piping Conference, American Society of Mechanical Engineers, 2015. V06BT06A076–-V06BT06A076.

[14] C.S. Wu, Q.X. Hu, J.Q. Gao, An adaptive heat source model for finite-element analysis of keyhole plasma arc welding, Comput. Mater. Sci 46 (1) (2009) 167–172.

[15] V.D. Fachinotti, A. Cardona, B. Baufeld, O. der Biest, Finite-element modelling of heat transfer in shaped metal deposition and experimental validation, Acta Mater. 60 (19) (2012) 6621–6630.

[16] A. Becker, A. Yaghi, State of the Art Review - Weld Simulation Using Finite Element Methods, 2004 Ph.D. thesis.

[17] M.C. Smith, O. Muránsky, C. Austin, P.J. Bendeich, L. Edwards, Optimised modelling of weld metal constitutive behaviour in the NeT TG4 international weld simulation and measurement benchmark, in: ASME 2012 Pressure Vessels and Piping Conference, American Society of Mechanical Engineers, 2012, pp. 1125–1137.

[18] I. Steinbach, M. Apel, Multi phase field model for solid state transformation with elastic strain, Physica D 217 (2) (2006) 153–160, doi:10.1016/j.physd.2006.04.001.

[19] I. Steinbach, F. Pezzolla, A generalized field method for multiphase transformations using interface fields, Physica D 134 (4) (1999) 385–393, doi:10.1016/S0167-2789(99)00129-3.

[20] H.-K. Kim, S.G. Kim, S. Wong, I. Steinbach, B.-J. Lee, Phase-field modeling for 3D grain growth based on a grain boundary energy database, Modell. Simul. Mater. Sci. Eng. 22 (3) (2014) 34004, doi:10.1088/0965-0393/22/3/034004.

[21] I. Steinbach, F. Pezzolla, B. Nestler, M. Seeßelberg, R. Prieler, G. Schmitz, J. Rezende, A phase field concept for multiphase systems, Physica D 94 (3) (1996) 135–147, doi:10.1016/0167-2789(95)00298-7.

[22] N. Moelans, B. Blanpain, P. Wollants, Quantitative phase-field approach for simulating grain growth in anisotropic systems with arbitrary inclination and misorientation dependence, Phys. Rev. Lett. 101 (2) (2008) 25502, doi:10.1103/PhysRevLett.101.025502.

[23] M. Courtois, M. Carin, P. Le Masson, S. Gaied, M. Balabane, A complete model of keyhole and melt pool dynamics to analyze instabilities and collapse during laser welding, J. Laser Appl. (2014), doi:10.2351/1.4886835.

[24] A. Ebrahimi, M. Sattari, S.J. Bremer, M. Luckabauer, G. willem R.B.E. Romer, I.M. Richardson, C.R. Kleijn, M.J. Hermans, The influence of laser characteristics on internal flow behaviour in laser melting of metallic substrates, Mater. Des. 214 (2022) 110385, doi:10.1016/j.matdes.2022.110385.

[25] C. Tang, K. Le, C. Wong, Physics of humping formation in laser powder bed fusion, Int. J. Heat Mass Transf. 149 (2020) 119172.

[26] C. Tang, L. Yao, H. Du, Computational framework for the simulation of multi material laser powder bed fusion, Int. J. Heat Mass Transf. 191 (2022) 122855.

[27] T. Flint, M. Anderson, V. Akrivos, M. Roy, J. Francis, A. Vasileiou, M. Smith, A fundamental analysis of factors affecting chemical homogeneity in the laser powder bed fusion process, Int. J. Heat Mass Transf. 194 (2022) 122985, doi:10.1016/j.ijheatmasstransfer.2022.122985.

[28] C. Panwisawas, Y. Sovani, R.P. Turner, J.W. Brooks, H.C. Basoalto, I. Choquet, Modelling of thermal fluid dynamics for fusion welding, J. Mater. Process. Technol. (2017), doi:10.1016/j.jmatprotec.2017.09.019.

[29] C. Panwisawas, C.L. Qiu, Y. Sovani, J.W. Brooks, M.M. Attallah, H.C. Basoalto, On the role of thermal fluid dynamics into the evolution of porosity during selective laser melting, Scr. Mater. 105 (2015) 14–17.

[30] S.A. Self, Focusing of spherical Gaussian beams, Appl. Opt. (1983), doi:10.1364/ao.22.000658.

[31] S. Hosseini, N. Darabiha, D. Thévenin, Mass-conserving advection-diffusion lattice boltzmann model for multi-species reacting flows, Physica. A 499 (2018) 40–57, doi:10.1016/j.physa.2018.01.034.

[32] H. Liu, J. Tang, L. Sun, Z. Mo, G. Xie, An assessment and analysis of phase change models for the simulation of vapor bubble condensation, Int. J. Heat Mass Transf. 157 (2020) 119924, doi:10.1016/j.ijheatmasstransfer.2020.119924.

[33] CRC handbook of chemistry and physics: a ready-reference book of chemical and physical data, Choice Reviews Online (2010), doi:10.5860/choice.47-3553.

[34] J. Dean, Lange's Handbook of Chemistry, 15th ed, 1999.

[35] Y. Zhang, J.R. Evans, S. Yang, Corrected values for boiling points and enthalpies of vaporization of elements in handbooks, J. Chem. Eng. Data (2011), doi:10.1021/je1011086.

[36] I. Mills, R. Jones, Quantities, units and symbols in physical chemistry, Vib Spectrosc (1990), doi:10.1016/0924-2031(90)80016-w.

[37] V. Klapczynski, M. Courtois, R. Meillour, E. Bertrand, D.L. Maux, M. Carin, T. Pierre, P.L. Masson, P. Paillard, Temperature and time dependence of manganese evaporation in liquid steels. multiphysics modelling and experimental confrontation, Scr. Mater. 221 (2022) 114944, doi:10.1016/j.scriptamat.2022.114944.